Retrieval of Sun Brightness Temperature and Precipitating Cloud Extinction Using Ground-Based Sun-Tracking Microwave Radiometry

Vinia Mattioli, *Member, IEEE*, Luca Milani, *Member, IEEE*, Kevin M. Magde, George A. Brost, and Frank S. Marzano, *Fellow, IEEE*

***Abstract*—Sun-tracking (ST) microwave radiometry is a technique where the Sun is used as a microwave signal source and it is here rigorously summarized. The antenna noise temperature of a ground-based microwave radiometer is measured by alternately pointing toward-the-Sun and off-the-Sun while tracking it along its diurnal ecliptic. During clear sky the brightness temperature of the Sun disk emission at K and Ka band and in the unexplored millimeter-wave frequency region at V and W band can be estimated by adopting different techniques. Using a unique dataset collected during 2015 through a ST multifrequency radiometer, the Sun brightness temperature shows a decreasing behavior with frequency with values from about 9000 K at K band down to about 6600 K at W band. In the presence of precipitating clouds the ST technique can also provide an accurate estimate of the atmospheric extinction up to about 32 dB at W band with the current radiometric system. Parametric prediction models for retrieving all-weather atmospheric extinction from ground-based microwave radiometers are then tested and their accuracy evaluated.**

***Index Terms*—Atmospheric extinction, ground-based microwave radiometry, microwave and millimeter-wave frequencies, Sun brightness temperature, Sun-tracking.**

I. Introduction

The Sun-tracking (ST) microwave (MW) radiometry technique consists in spatially varying the observation angle on and off the Sun by means of a ground-based radiometer antenna [1], [2]. In this respect, ST uses the Sun as a signal source of radiation transmitting through the atmosphere [1]. The interest of the ST microwave radiometry is typically twofold. First, by properly choosing the switching time interval and taking into account the main lobe aperture under clear-sky conditions, it is possible to estimate the effective brightness temperature of the Sun, which is a valuable data in radio astronomy [3]. Second, the ST technique allows the retrieval of the atmospheric extinction in all weather conditions with an upper limit depending on the radiometric accuracy [4].

In radioastronomy MW observations of the Sun are dominated by large multielement arrays [5], which have the advantage of high spatial resolution, high sensitivity, and ability to make maps on very short timescales, discriminating the rather weak signal of the quiet Sun from the strong active region signals [6]. Indeed, most solar radio observations have focused on active region phenomena such as flares and coronal mass ejections, demonstrating powerful diagnostic capabilities of large microwave arrays to address open issues regarding the quiet Sun [7], [8]. At submillimeter frequencies Sun observations have historically been performed with single-dish antennas thus showing comparatively a poorer spatial resolution [9]. Solar measurements at multiple frequencies are useful as the emitted brightness arises from different layers of the solar atmosphere. For instance, the lower chromosphere is typically detected at frequencies of 100–1000 GHz, the middle chromosphere at 20–100 GHz, and the upper chromosphere at frequencies of 2–20 GHz. The solar corona is usually measured at frequencies of 2 GHz and below [3].

The application of a ST microwave radiometry technique for the retrieval of the atmospheric properties was envisaged in early works to complement Sun observations with radiotelescopes [10]. In the seventies Hogg and Chu [11] proposed the ST technique as an independent way to measure rain attenuation with a good dynamic range. Shimada *et al*. [12] proposed a method to provide clear-sky absorption statistics. The potential of ground-based MW radiometry in radiopropagation and remote sensing applications has been also demonstrated by Marzano *et al*. [4], [13], who proposed it to develop and validate retrieval models for estimating the total atmospheric extinction due to precipitation and its associated rainfall rate [14]–[16]. However, the difficulty to assess the capability of ground-based MW radiometry for atmospheric parameter estimation is typically linked to the lack of collocated beacon measurements at the same observation frequency [17]. In this respect, ST microwave radiometry is a self-consistent approach where atmospheric path attenuation estimates can be also verified in almost all weather conditions and even in the unexplored range of millimeter and submillimeter wavelengths.

A few operational ST multifrequency microwave radiometers are currently operational. One of these is the system recently

Manuscript received July 1, 2016; revised September 30, 2016 and November 9, 2016; accepted November 13, 2016. This work was supported in part by the EOARD HiRadProp project within the US-AFL EOARD program and in part by the Sapienza University of Rome, Rome, Italy. *(Corresponding author: Vinia Mattioli.)*

V. Mattioli is with the HE-Space, Darmstadt 64293, Germany, and also with the Center of Excellence CETEMPS, University of L'Aquila, L'Aquila 67100, Italy (e-mail: vinia.mattioli@eumetsat.it).

L. Milani and F. S. Marzano are with the Department of Information Engineering, Sapienza University of Rome, Rome 00184, Italy, and also with the Center of Excellence CETEMPS, University of L'Aquila, L'Aquila 67100, Italy (e-mail: luca.milani@uniroma1.it; marzano@diet.uniroma1.it).

K. M. Magde and G. A. Brost are with the Air Force Research Laboratory, Rome, NY 13440 USA (e-mail: kevin.magde@us.af.mil; george.brost@us.af.mil).

Color versions of one or more of the figures in this paper are available online at http://ieeexplore.ieee.org.

Digital Object Identifier 10.1109/JSTARS.2016.2633439

installed in Rome (NY, USA) at Air Force Research Laboratory (AFRL) [34]. This AFRL ST-microwave radiometer (ST-MWR) has four channels with receivers at K band (23.8 GHz), Ka (31.4 GHz), V band (72.5 GHz), and W band (82.5 GHz) and is a modified version of a commercial water-vapor and cloud-liquid MWR series [23], to allow us an automatic Sun-switching and tracking operation mode. A unique relatively long dataset has been collected by the AFRL ST MWR in 2015. These data represent an opportunity to test ground-based single-antenna ST for both radioastronomy and radiopropagation. Moreover, as an additional application, ST microwave radiometry can be used as a system calibration tool to determine receiving systems noise temperature [18] as well as antenna boresight pointing errors [19].

This work has several purposes: 1) to summarize the basics of ST microwave radiometry by investigating the issues of antenna pattern beam-filling, error sensitivity, and estimate limitations; 2) to illustrate the data processing of the AFRL available measurements in 2015 and the need to apply proper radiometric approaches to exploit ST potential; 3) to estimate the brightness temperature of the Sun at K, Ka, V, and W band using the collected dataset at AFRL in 2015 and comparing with available radioastronomical data; 4) to propose the parametric retrieval of the atmospheric extinction at K, Ka, V, and W band due to precipitating clouds and validating it with ST measurements in different weather conditions.

The paper is structured as follows. In Section II two different techniques, based on elevation scanning and surface meteorological data, are rigorously proposed to estimate the Sun brightness temperature and the atmospheric extinction from ST-MWR measurements. Section III is devoted to the description, quality control, and processing of the available ST-MWR data. Section IV describes the application of the two methodologies for the Sun brightness temperature estimate and discusses the results. Section V shows the retrieval of atmospheric extinction in cloudy and precipitating conditions. Finally, in Section VI conclusions are discussed. Sensitivity and error budget analyses are carried out in the Appendix, with respect to antenna pattern, beam filling, atmospheric attenuation uncertainties, and instrument spectral response.

II. ST Microwave Radiometry

Considering ground-based observations, the measured antenna noise temperature T_A along the radiometer antenna pointing angle (θ_0, φ_0) is the convolution between the received sky brightness temperature and the normalized antenna power radiation pattern $F_n(\theta_0, \varphi_0, \theta, \varphi)$ [20]:

$$T_A(\theta_0, \varphi_0) = \frac{\int_{4\pi} T_B(\theta, \varphi) F_n(\theta_0, \varphi_0, \theta, \varphi)\, d\Omega}{\int_{4\pi} F_n(\theta_0, \varphi_0, \theta, \varphi)\, d\Omega} \tag{1}$$

with

$$\int_{4\pi} F_n(\theta_0, \varphi_0, \theta, \varphi)\, d\Omega = \Omega_{\mathrm{Pant}} \tag{2}$$

where Ω_{Pant} is the antenna radiation-pattern solid angle. All the involved parameters are also dependent on frequency, which is neglected in the formulations in favor of geometric considerations.

When pointing out-of-the-Sun (*ooS*), the sky brightness temperature $T_{B\mathrm{ooS}}$, impinging upon the antenna along the zenith angle θ and azimuth φ [20], can be written as

$$T_{B\mathrm{ooS}}(\theta, \varphi) = T_{\mathrm{mr}}(\theta, \varphi)\left[1 - e^{-\tau(\theta,\varphi)}\right] + T_{\cos} e^{-\tau(\theta,\varphi)} \tag{3}$$

where T_{mr} is the sky mean radiative temperature (that can be defined in all-weather conditions [17], [36]), τ is the atmospheric optical thickness (in Neper), and $T_{\cos}$ is the brightness temperature of the cosmic background (equal to about 2.73 K).

When pointing at the Sun, the toward-the-Sun (*twS*) sky brightness temperature $T_{B\mathrm{twS}}$ is given by the sum of two components, the Sun brightness temperature $T_{B\mathrm{sun}}$, attenuated by the atmosphere, and the brightness temperature of the sky

$$T_{B\mathrm{twS}}(\theta, \varphi) = T_{B\mathrm{sun}} e^{-\tau(\theta,\varphi)} + T_{\mathrm{mr}}(\theta, \varphi)\left[1 - e^{-\tau(\theta,\varphi)}\right] + T_{\cos} e^{-\tau(\theta,\varphi)}. \tag{4}$$

According to (1), the computation of the antenna noise temperature $T_{A\mathrm{twS}}$, measured observing the Sun, implies that the $T_{B\mathrm{twS}}$ is observed by the antenna within the solid angle Ω_{sun} subtended by the Sun. Therefore, it holds:

$$\begin{aligned} T_{A\mathrm{twS}}(\theta_0, \varphi_0) = {} & \frac{1}{\Omega_{\mathrm{Pant}}} \int_{\Omega_{\mathrm{sun}}} \Big[T_{B\mathrm{sun}} e^{-\tau(\theta,\varphi)} + T_{\mathrm{mr}}(\theta, \varphi) \\ & \times \left(1 - e^{-\tau(\theta,\varphi)}\right) + T_{\cos} e^{-\tau(\theta,\varphi)}\Big] \\ & \times F_n(\theta_0, \varphi_0, \theta, \varphi) d\Omega + \frac{1}{\Omega_{\mathrm{Pant}}} \\ & \times \int_{4\pi - \Omega_{\mathrm{sun}}} \Big(T_{\mathrm{mr}}(\theta, \varphi)\left[1 - e^{-\tau(\theta,\varphi)}\right] \\ & + T_{\cos} e^{-\tau(\theta,\varphi)}\Big) \cdot F_n(\theta_0, \varphi_0, \theta, \varphi)\, d\Omega \end{aligned} \tag{5}$$

which can be rewritten as:

$$\begin{aligned} T_{A\mathrm{twS}}(\theta_0, \varphi_0) = {} & \frac{1}{\Omega_{\mathrm{Pant}}} \int_{\Omega_{\mathrm{sun}}} T_{B\,\mathrm{sun}} e^{-\tau(\theta,\varphi)} \\ & \cdot F_n(\theta_0, \varphi_0, \theta, \varphi)\, d\Omega + \frac{1}{\Omega_{\mathrm{Pant}}} \\ & \times \int_{4\pi} \Big(T_{\mathrm{mr}}(\theta, \varphi)\left[1 - e^{-\tau(\theta,\varphi)}\right] \\ & + T_{\cos} e^{-\tau(\theta,\varphi)}\Big) F_n(\theta_0, \varphi_0, \theta, \varphi)\, d\Omega. \end{aligned} \tag{6}$$

It is useful to introduce the beam-filling factor f_Ω as the ratio between the Sun radiation-pattern solid angle $\Omega_{\mathrm{P\,sun}}$ and the antenna beamwidth radiation-pattern solid angle Ω_{Pant}, it holds

$$f_\Omega = \frac{\int_{\Omega_{\mathrm{sun}}} F_n(\theta_0, \varphi_0, \theta, \varphi)\, d\Omega}{\Omega_{\mathrm{Pant}}} = \frac{\Omega_{\mathrm{P\,sun}}}{\Omega_{\mathrm{Pant}}}. \tag{7}$$

If it is assumed that the Sun has a uniform brightness temperature within the beam (e.g., Ω_{sun} is much smaller than the antenna main beam half-power solid angle), then, using (7), we can approximate (6) as

$$T_{A_{\mathrm{twS}}}\left(\theta_0,\varphi_0\right) \cong f_\Omega T_{B\ \mathrm{sun}} e^{-\tau(\theta_0,\varphi_0)} + T_{\mathrm{mr}}\left(\theta_0,\varphi_0\right) \times \left[1-e^{-\tau(\theta_0,\varphi_0)}\right] + T_{\cos} e^{-\tau(\theta_0,\varphi_0)}. \quad (8)$$

In ground-based radiometry, it is also commonly assumed that the atmospheric contribution is constant within the main beam and $T_{A\mathrm{ooS}}$ is approximated by the $T_{B\mathrm{ooS}}$ at (θ_0, φ_0).

Analogously, for the *ooS* mode, we can simplify

$$\begin{aligned} T_{A\mathrm{ooS}}\left(\theta_0,\varphi_1\right) &= \frac{1}{\Omega_{\mathrm{Pant}}}\int_{4\pi}\left(T_{\mathrm{mr}}\left(\theta,\varphi\right)\left[1-e^{-\tau(\theta,\varphi)}\right] + T_{\cos}e^{-\tau(\theta,\varphi)}\right) F_n\left(\theta_0,\varphi_1,\theta,\varphi\right)d\Omega \\ &\cong T_{\mathrm{mr}}\left(\theta_0,\varphi_1\right)\left[1-e^{-\tau(\theta_0,\varphi_1)}\right] + T_{\cos}e^{-\tau(\theta_0,\varphi_1)}. \end{aligned} \quad (9)$$

In the ST technique, the radiometer antenna is pointing alternatively on and off the Sun, and between these two measurements, the elevation angle θ_0 is kept constant, while the azimuth angle is switched from φ_0 (twS) to φ_1 (ooS). Then, after a few observations, the elevation angle is varied, in accordance with the Sun movement along its diurnal ecliptic.

The ST antenna noise temperature difference for each pointing angle can then be expressed by:

$$\Delta T_A\left(\theta_0,\varphi_0,\varphi_1\right) = T_{A\mathrm{twS}}\left(\theta_0,\varphi_0\right) - T_{A\mathrm{ooS}}\left(\theta_0,\varphi_1\right). \quad (10)$$

If the switching between *ooS* and *twS* observation modes is fast enough and the azimuth distance is chosen so that the Sun is just outside the field of view of the instrument, it can be assumed that the mean radiative temperature and optical thickness do not change between the two observation modes (i.e., $T_{\mathrm{mr}}(\theta_0,\varphi_0) \cong T_{\mathrm{mr}}(\theta_0,\varphi_1)$ and $\tau(\theta_0,\varphi_0) \cong \tau(\theta_0,\varphi_1)$). Substituting (8) and (9) into (10) we obtain:

$$\Delta T_A\left(\theta_0,\varphi_0\right) \cong f_\Omega\left(\theta_0,\varphi_0\right) T_{B\ \mathrm{sun}} e^{-\tau(\theta_0,\varphi_0)} \quad (11)$$

where the beam-filling factor f_Ω depends on the pointing angle. Previous equation gives the basis for estimating $T_{B\ \mathrm{sun}}$ and the atmosphere path attenuation, as described in Section II-A and II-B.

A. *Estimation of Sun Brightness Temperature in Clear Sky*

During clear-sky conditions, the ST technique can be used to estimate the brightness temperature $T_{B\,\mathrm{sun}}$ emitted by the Sun. Two different approaches can be applied: 1) the Langley elevation-based self-consistent method and 2) the $T_{\mathrm{mr}}-$based meteorologically-oriented method. Both methods are able to provide reliable results with the availability of radiometric measurements in clear air conditions, when $T_{B\,\mathrm{sun}}$ estimates are less affected by the atmosphere variability. In both methods, a plane-parallel horizontally stratified and azimuthally homogeneous atmosphere is assumed and the "*secant law*" is applied to describe the elevation angle dependence of the optical thickness.

The *Langley technique* is commonly used in Sun-photometry for determining the Sun radiance at the top of the atmosphere with ground-based instruments [1], [2]. It exploits the antenna noise temperature difference in (11) according to:

$$\begin{aligned} \ln\left[\Delta T_A\left(\theta_0\right)\right] &= \ln\left[f_\Omega T_{B\ \mathrm{sun}}\right] - \tau\left(\theta_0\right) \\ &= \ln\left[T^*_{B\ \mathrm{sun}}\right] - \tau_z\ m\left(\theta_0\right) \end{aligned} \quad (12)$$

where $T^*_{B\ \mathrm{sun}}$ is the brightness temperature of the Sun weighted by the filling factor f_Ω and $m(\theta_0)$ stands for atmospheric air mass, equal to $\sec(\theta_0)$. Under the plane-parallel atmosphere assumption, it holds that $\ln[\Delta T_A(\theta_0)]$ is linearly dependent on the air mass $m(\theta_0)$ and we can estimate $T^*_{B\ \mathrm{sun}}$ through the exponential of the intercept of the linear best-fitting curve. Finally, exploiting the beam-filling factor f_Ω, as given in (7), the sun brightness temperature $T_{B\ \mathrm{sun}}$ is computed:

$$\ln\left[\Delta T_A\left(\theta_0\right)\right] = a + bm\left(\theta_0\right) \quad \rightarrow \quad T_{B\ \mathrm{sun}} = \frac{T^*_{B\ \mathrm{sun}}}{f_\Omega} = \frac{\exp\left(a\right)}{f_\Omega}. \quad (13)$$

The *meteorological technique* is based on the radiometer (9) in clear air [1], [34]. In a horizontally-stratified clear air, we can obtain the atmospheric extinction $\tau(\theta_0)$ according to:

$$\tau\left(\theta_0\right) = \ln\left[\frac{T_{\mathrm{mr}}\left(\theta_0\right) - T_{\cos}}{T_{\mathrm{mr}}\left(\theta_0\right) - T_{A\mathrm{ooS}}\left(\theta_0\right)}\right]. \quad (14)$$

In (14), the mean radiating temperature T_{mr} of the atmosphere is needed. It can be interpolated from concurrent radiosonde observation (RaOb) or estimated directly from surface temperature T_s, pressure p_s, and relative humidity RH_s in clear air [21], [22]. Details on the computation of the T_{mr} are given in Section III-B. From (11), using the ST measurements, the Sun brightness temperature is computed according to:

$$T_{B\ \mathrm{sun}} = \frac{T^*_{B\ \mathrm{sun}}}{f_\Omega} = \frac{1}{f_\Omega}\left(\Delta T_A\left(\theta_0\right)\cdot e^{\tau(\theta_0)}\right). \quad (15)$$

Note that, with respect to the Langley technique, which provides one estimate from the fitted regression line, the meteorological technique provides a time series of $T_{B\ \mathrm{sun}}$.

In order to compute $T_{B\ \mathrm{sun}}$, the filling factor f_Ω in (7) must be evaluated. Note that the Sun radiation-pattern solid angle $\Omega_{\mathrm{P\ sun}}$ can be computed according to (7):

$$\Omega_{\mathrm{P\ sun}} = \int_{\Omega_{\mathrm{sun}}} F_n\left(\theta_0,\varphi_0,\theta,\varphi\right)d\Omega. \quad (16)$$

A typical assumption is that $F_n(\theta_0,\varphi_0,\theta,\varphi) \cong 1$ over Ω_{sun}, so that the effect of the radiometer antenna pattern can be neglected. In this case the filling factor is given by $f_\Omega \cong \Omega_{\mathrm{sun}}/\Omega_{\mathrm{ant}}$ being $\Omega_{\mathrm{P\ sun}} \cong \Omega_{\mathrm{sun}}$. The Sun solid angle Ω_{sun} can be then obtained from:

$$\Omega_{\mathrm{sun}} \cong \frac{\pi}{4}\Theta^2_{\mathrm{sun}} \cong \frac{\pi r^2_{\mathrm{sun}}}{R^2_{\mathrm{ES}}} \quad (17)$$

where r_{sun} is the radius of the Sun, approximated as a circular disk, and R_{ES} is the Earth–Sun average distance, and Θ_{sun} is the zenithal-plane angle subtended by the Sun. The last right-hand side term of (17) is obtained by approximating the solid angle as the ratio between the object cross area and its square distance.

However, if the antenna beamwidth cross section is comparable with the diameter of the Sun, such assumption is no longer valid. To account for it, a Gaussian shape has been used to model the radiometer antenna normalized pattern $F_{n\mathrm{ML}}$ main beam, as suggested by the radiometer manufacturer [23]. Thus, we can express $F_{n\mathrm{ML}}$ as [27]:

$$F_{n\mathrm{ML}}(\theta,\varphi) = e^{-\ln(2)\left(2\frac{\theta}{\Theta_{\mathrm{ML}}}\right)^2} \tag{18}$$

where Θ_{ML} is the half-power beamwidth of the antenna main beam. Then, assuming $\sin\theta \cong \theta$:

$$\Omega_{\mathrm{P\ sun}} = \int_0^{2\pi}\int_0^{\frac{\Theta_{\mathrm{sun}}}{2}} F_{n\mathrm{ML}}(\theta,\varphi)\ \sin\theta d\theta d\varphi \cong \frac{\pi}{4\ln(2)}\Theta_{\mathrm{ML}}^2\left[1 - e^{-\ln(2)\left(\frac{\Theta_{\mathrm{sun}}}{\Theta_{\mathrm{ML}}}\right)^2}\right]. \tag{19}$$

The antenna radiation-pattern solid angle Ω_{Pant} can be obtained from (2) by considering the antenna main beam efficiency η_{ML} and calculating the antenna main lobe radiation-pattern solid angle Ω_{PML} for the Gaussian-shape beam in (18)

$$\Omega_{\mathrm{Pant}} = \frac{\Omega_{\mathrm{PML}}}{\eta_{\mathrm{ML}}} = \frac{\int_{4\pi} F_{n\mathrm{ML}}(\theta,\varphi)\, d\Omega}{\eta_{\mathrm{ML}}} \cong \frac{1}{\eta_{\mathrm{ML}}}\frac{\pi}{4\ln(2)}\Theta_{\mathrm{ML}}^2\left[1 - e^{-\ln(2)\left(\frac{2\pi}{\Theta_{\mathrm{ML}}}\right)^2}\right] \cong \frac{1}{\eta_{\mathrm{ML}}}\frac{\pi}{4\ln(2)}\Theta_{\mathrm{ML}}^2 \tag{20}$$

where η_{ML} is defined as the ratio between the main lobe radiation solid angle and the antenna one. It is possible to neglect the exponential term for Θ_{ML} values up to 20°.

Summarizing, the expression of the filling factor f_{Ω} is obtained from the following expression:

$$f_{\Omega} = \eta_{\mathrm{ML}}\left[1 - e^{-\ln(2)\left(\frac{\Theta_{\mathrm{sun}}}{\Theta_{\mathrm{ML}}}\right)^2}\right] \tag{21}$$

using (19) and (20). The possible effects of antenna pattern side lobes are modeled and discussed in the Appendix.

B. *Atmospheric Extinction in Precipitating Clouds*

Starting from (11), provided that estimates of $T^*_{B\ \mathrm{sun}}$ are available for instance from ST measurements obtained during clear sky, the extinction A_{ST} (in dB) in all weather conditions can be retrieved from the ΔT_A differences between *ooS* and *twS* measurements, according to

$$A_{\mathrm{ST}}(\theta_0,\varphi_0) = 4.343\,\tau(\theta_0,\varphi_0) = 4.343\,\ln\left[\frac{T^*_{B\ \mathrm{sun}}(\theta_0,\varphi_0)}{\Delta T_A(\theta_0,\varphi_0)}\right]. \tag{22}$$

In the presence of clouds or precipitation, as the atmospheric extinction significantly increases, the Sun signal is also increasingly attenuated, and therefore the antenna noise temperature difference between the two measurement modes *ooS* and *twS* decreases. For heavy precipitation, the contribution of the Sun is completely masked by the rain attenuation and the ΔT_A differences are only dependent on the radiometer noise and the atmosphere variability, providing an upper limit to the application of the technique for the retrieval of rain attenuation [4].

III. Measurement Dataset

The available dataset consists of 163 days of measurements collected by the ground-based AFRL ST-MW radiometer from May to October 2015 in Rome, NY, USA (43.2°N, 75.4°W) at angles between 20° and 70°. The AFRL ST-MWR has four channels with receivers at 23.8, 31.4, 72.5, and 82.5 GHz and is a modified version of the RPG LPW-U72-82 water-vapor and cloud-liquid MWR [23], [28]. It is provided with an azimuth positioner allowing a scan step of 0.15° in elevation and 0.1° in azimuth. The track of the Sun along the ecliptic is based on input data (latitude, longitude, time) and it is performed in a Sun-switching operation mode, keeping the elevation angle θ_0 constant, and varying the azimuth angle from φ_0 (twS) to φ_1 (ooS) according to (10). The integration time of each measurement is set to 1 s and the azimuth positioner switches every 6 s in order to perform the integration with fixed antenna position. The processing and quality-control procedures applied to the radiometer data are described in the following.

A. *Clear-Air Data Discrimination*

Both Langley and meteorological techniques need measurements in clear-sky to estimate $T_{B\ \mathrm{sun}}$. The discrimination has been carried out through a scalar quantity named Status Sky Indicator (SSI), purely based on the measured brightness temperatures. The method has been successfully applied in several applications with ground-based radiometers [29], [30]. SSI is defined as

$$\mathrm{SSI}(\theta_0) = \frac{T_{A\mathrm{ooS}(31.4\ \mathrm{GHz})}(\theta_0) - c(\theta_0)}{T_{A\mathrm{ooS}(23.8\ \mathrm{GHz})}(\theta_0)} \tag{23}$$

with

$$c(\theta_0) = -0.13\ \mathrm{m}^2 + 6.3\ \mathrm{m} + 2.1 \tag{24}$$

where c is a parameter dependent on air mass $m = \sec(\theta_0)$ and θ_0 is the elevation angle. A clear air condition is assumed if SSI is less than a given threshold $\mathrm{SSI_{th}}$ given by

$$\mathrm{SSI_{th}}(\theta_0) = -0.00012\ \mathrm{m}^2 + 0.0066\ \mathrm{m} + 0.31. \tag{25}$$

A clear-sky day is assumed if the number of measurements for which the SSI value is below the threshold is larger than the 98% of available samples (neglecting the non-clear-air samples in the $T_{B\ \mathrm{sun}}$ estimation).

Table I details the available measurement dataset providing a monthly classification in terms of clear, cloudy, and rainy days. The clear-air days have been identified by using the SSI criterion as described before, whereas the discrimination of rainy days has been carried out by looking at the rain flag directly provided by the radiometer.

B. *Radiosounding Dataset*

SSI parameterization in (23) has been set up by performing radiative transfer simulations of brightness temperatures at 23. 8 and 31.4 GHz at several elevation angles applied to a long-term

TABLE I
MONTHLY CLASSIFICATION OF CLEAR, CLOUDY, AND RAINY DAYS DURING AFRL ST-MWR AVAILABLE MEASUREMENTS

Month	Clear	Cloudy	Rainy	Total
May 2016	5	13	4	22
June 2016	0	19	10	29
July 2016	2	22	7	31
August 2016	0	21	6	27
September 2016	1	21	8	30
October 2016	7	12	5	24

available RaOb dataset. The closest RaOb site to Rome, NY, USA, is located at Albany County Airport, NY, USA (WMO station ID code 72518, WBAN ID code 14735). RaOb data belonging to the period 1994–2012 have been collected for this study. Downwelling brightness temperatures have been generated using a plane parallel radiative transfer equation (RTE) scheme [31] with an updated version of Rosenkranz [32] for gas absorption and a cloud model as given in [33].

The RaOb dataset has been also used to generate corresponding mean radiating temperatures $T_{\rm mr}$ at the same frequencies and angles. Monthly regression coefficients for each frequency and angle were computed to relate $T_{\rm mr}$ values to the surface temperature T_s, pressure p_s, and relative humidity RH_s provided by the radiosondes:

$$T_{\rm mr}(\theta_0) = a_0(\theta_0) + a_1(\theta_0)\,T_s + a_2(\theta_0)\,p_s + a_3(\theta_0)\,\mathrm{RH}_s \tag{26}$$

where the regression coefficients a_i are dependent on the elevation angle θ_0. Finally, the regression coefficients have been fitted with respect to air mass *m* to provide the final coefficients a_i. Those coefficients were then applied to the concurrent surface measurements from the meteorological sensors that are part of the radiometer equipment.

C. Filtering Toward-the-Sun Observations in Clear Air

The maximum $T_{A_{\rm twS}}$ values were held on for each elevation angle to compute $T_{B\ \rm sun}$ with both Langley and Meteorological technique. AFRL-MWR ST mode maintains a constant elevation for a certain time and the Sun does not remain stationary during that period. The best matching observation corresponds to the maximum value, where the Sun disk is centered with respect to the antenna beamwidth. Only for the Langley technique, a binning average with respect to air mass (steps of 0.1) was performed to achieve an equal distribution of samples with airmass and not to influence the linear regression in (13).

D. Evaluation of Antenna Beamwidth

The AFRL MWR antenna is a feedhorn/parabola system shaped to reduce the sidelobes to less than –30 dB at K-band and less than –40 dB at V and W band [23]. The antenna radiation pattern results approximately Gaussian, following the approximation given in (18). In order to evaluate the filling factor in (21), both the Sun disk angle $\Theta_{\rm sun}$, and the half-power beamwidth $\Theta_{\rm 3dB}$ values must be retrieved [34]. Higher

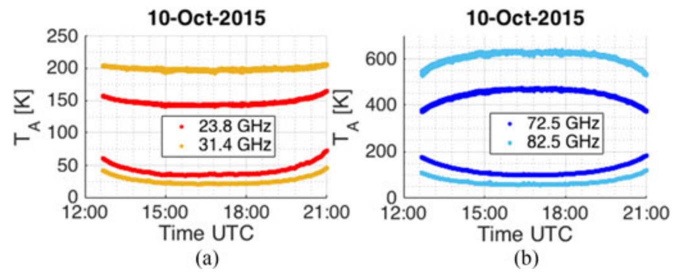

Fig. 1. Time series of ST-MWR measurements in terms of antenna noise temperatures for a case studies referring to a clear air (October 10, 2015) at the four AFRL-MWR available frequencies. (a) 23.8 and 31.4 GHz. (b) 72.5 and 85.5 GHz.

accuracy is needed in knowing $\Theta_{\rm ML}$ exact values with respect to the ones provided by RPG LPW-U72-82 technical specifications (3.7°, 3.3°, 1.3°, and 1.3°, at 23.8, 31.4, 72.5, and 82.5 GHz, respectively). The radiation pattern has been measured by scanning the radiometer across the Sun, i.e., letting the Sun drift across the radiometer path. From the known ephemeris, it has been possible to determine the relative angular position of the Sun assuming a uniform disk $\Theta_{\rm sun}$ of 0.533° arch. Finally, the measured brightness temperatures have been fit to a Gaussian profile convolved with the sun to obtain $\Theta_{\rm ML}$ measurements for each frequency. The AFRL full-width half-power beamwidth values are equal to 3.74°, 2.97°, 1.47°, and 1.30° at 23.8, 31.4, 72.5, and 82.5 GHz, respectively, with a main beam efficiency $\eta_{\rm ML}$ of 0.969 at Ka band and 0.979 at V and W band [24]. In the appendix, detailed theoretical sensitivity analysis and error budget have been reported, with particular emphasis on side lobe contributions.

IV. SUN BRIGHTNESS TEMPERATURE ESTIMATES

The analysis of the measured antenna noise temperature time series can give an insight on the ST concept and MW radiometric data behavior. Fig. 1 shows the time series of ST T_A measurements of both *ooS* (lower curves) and *twS* (upper curves) for the case study of October 10, 2015 at the four AFRL-MWR available frequencies. The trend observed at 23.8 and 31.4 GHz with respect to elevation [see Fig. 1(a)] is similar for both $T_{A\rm ooS}$ and $T_{A_{\rm twS}}$: at the beginning of the daily Sun-tracking, higher $T_{\rm A}$ values are observed at low elevation due to a larger atmospheric contribution, reaching their minimum at the solar noon (i.e., maximum tracking elevation).

In Fig. 1(b), the time series at 72.5 and 82.5 GHz shows an opposite trend with elevation for $T_{A\rm ooS}$ and $T_{A_{\rm twS}}$, with the latter reaching their maximum values at the solar noon. Such behavior is explained by recalling (8) and the increasing impact of $T^*_{B\ \rm sun}$ contribution at K, Ka and V, W band, because of the increasing filling factor f_Ω. At K and Ka band, the atmospheric contribution with air mass still dominates over that one due to the Sun, whereas in V and W band it is the reverse. The behavior in the presence of clouds or precipitation is described in Section V.

Fig. 2 shows the estimate of $T^*_{B\ \rm sun}$ using the Langley technique for each frequency and for the case study of October 10, 2015, exploiting the natural logarithm of the antenna noise

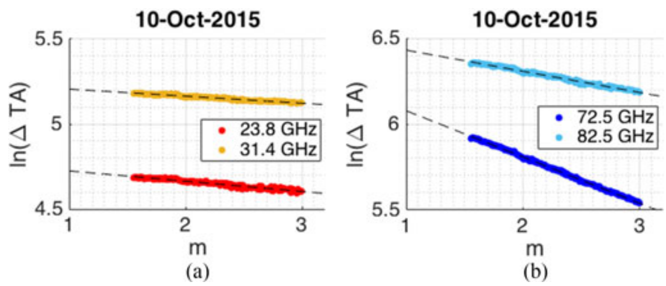

Fig. 2. Estimate of $T^*_{B\,\mathrm{sun}}$ using the Langley technique (128 samples equally spaced in terms of air mass), as discussed in Section II-B, for each frequency on October 10, 2015. (a) 23.8 ($R^2 = 0.9367$) and 31.4 GHz ($R^2 = 0.9630$). (b) 72.5 ($R^2 = 0.9984$) and 85.5 GHz ($R^2 = 0.9909$).

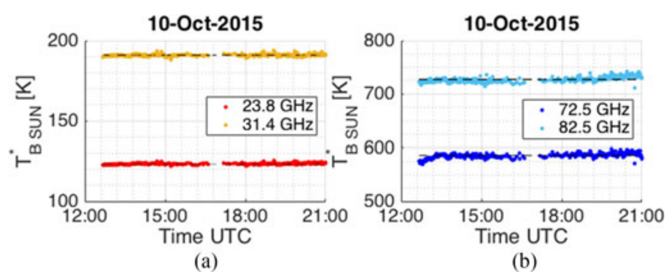

Fig. 3. Estimates of $T^*_{B\,\mathrm{sun}}$ using the meteorological technique for each frequency on October 10, 2015.

temperature difference versus air mass. The fitted linear regressions are shown as black dashed lines, and R-squared statistics are also given. As discussed in Section II-A, $T^*_{B\,\mathrm{sun}}$ is computed according to (13) from the intercept of the fitted line, while the slope is an estimate of the daily average atmospheric zenith extinction. Fig. 3 shows the estimate of $T^*_{B\,\mathrm{sun}}$ for October 10, 2015, by using the meteorological technique for each frequency. The average values of $T^*_{B\,\mathrm{sun}}$ are also shown as black dashed lines.

Daily $T^*_{B\,\mathrm{sun}}$ estimates obtained by the two techniques for all the available clear-sky dataset are given in Table II. Then, $T_{B\,\mathrm{sun}}$ values were computed by diving those estimates by the Sun filling factor f_Ω. The average estimates for both $T^*_{B\,\mathrm{sun}}$ and $T_{B\,\mathrm{sun}}$ are given in Table III. The values of the estimated beam filling factors are also reported and these were computed using AFRL-derived values described in Section III-D.

Table IV reports minimum and maximum deviations of the 15 examined clear-air days for both techniques. A standard deviation (std) over the daily time series has been carried out to provide the Meteorological deviation. To put deviations on a comparable scale, the Langley deviations have been computed supposing a Normal-distributed percentile associated to the linear regression in (13). By evaluating the 68.27% confidence intervals we are able to obtain deviation values equivalent to the Meteorological ones.

When comparing the Langley and the meteorological methods, we note that they provide very similar results. Differences exist because of the assumptions underlying their applicability. In the Langley technique, the daily attenuation variability affects the slope estimations and in turns the intercept (ideally, it should be independent as air mass is extrapolated to zero). As such, only the most stable days in clear-sky can be used for the estimate. Conversely, the meteorological technique has fewer constraints, with the price that it provides much larger uncertainty to the associated average value. The advantage of the Langley technique is that it is a stand-alone method, without the need of resorting to RTE models or the need of additional ancillary measurements.

The estimated $T_{B\,\mathrm{sun}}$ values decrease with increasing frequency ranging from about 9000 K down to about 6600 K. These values are consistent with those from radiotelescope observations [5], [18], and models [35]. $T_{B\,\mathrm{sun}}$ values at W band agree with a radiation originating from the Sun lower chromosphere. In particular, K-band measurements are available in previous researches: 1) comparing the result at 23.8 GHz in Table III with

TABLE II
LANGLEY AND METEOROLOGICAL DAILY ESTIMATES OF $T^*_{B\,\mathrm{sun}}$

LANGLEY $T^*_{B\,\mathrm{sun}}$ [K]				
	23.8 GHz	31.4 GHz	72.5 GHz	82.5 GHz
06/05/15	121.70	185.99	590.18	745.83
08/05/15	120.54	182.17	573.24	716.34
21/05/15	122.16	184.11	578.43	727.40
23/05/15	120.71	182.49	563.58	703.72
24/05/15	117.69	179.05	545.31	681.66
03/07/15	122.04	181.61	559.67	710.62
16/07/15	118.18	178.29	566.02	711.41
26/09/15	122.19	191.52	586.17	729.72
02/10/15	122.45	189.36	578.12	706.84
08/10/15	122.59	193.28	586.96	727.22
10/10/15	119.79	189.91	571.63	702.97
11/10/15	122.56	193.01	587.58	728.51
15/10/15	122.70	192.86	587.14	727.15
23/10/15	120.76	186.50	572.84	698.24
26/10/15	121.74	188.88	582.65	712.93
METEOROLOGICAL $T^*_{B\,\mathrm{sun}}$ [K]				
	23.8 GHz	31.4 GHz	72.5 GHz	82.5 GHz
06/05/15	124.05	189.68	564.22	704.09
08/05/15	121.64	185.33	570.65	710.55
21/05/15	119.84	184.21	571.80	709.88
23/05/15	119.66	184.29	570.71	707.81
24/05/15	119.62	183.63	567.61	707.61
03/07/15	120.44	184.48	565.26	705.74
16/07/15	119.74	184.19	564.30	703.32
26/09/15	123.86	191.05	589.66	730.19
02/10/15	124.26	190.89	592.92	723.28
08/10/15	123.59	191.30	582.63	726.86
10/10/15	123.47	190.93	585.69	727.18
11/10/15	124.56	192.41	593.56	734.70
15/10/15	124.56	191.80	581.76	729.38
23/10/15	124.17	190.58	602.84	735.99
26/10/15	123.77	190.03	586.08	726.32

TABLE III
LANGLEY AND METEOROLOGICAL AVERAGE ESTIMATE INTERCOMPARISON

		Langley		Meteorological	
f [GHz]	f_Ω	$T^*_{B\,\mathrm{sun}}$ [K]	$T_{B\,\mathrm{sun}}$ [K]	$T^*_{B\,\mathrm{sun}}$ [K]	$T_{B\,\mathrm{sun}}$ [K]
23.8	0.0136	121.19	8942	122.48	9037
31.4	0.0214	186.60	8719	188.32	8799
72.5	0.0853	575.30	6741	579.31	6788
82.5	0.1078	715.37	6638	718.86	6670

TABLE IV
LANGLEY AND METEOROLOGICAL ESTIMATE DEVIATIONS INTERCOMPARISON

	Langley Deviation		Meteorological Deviation	
f [GHz]	Min [K]	Max [K]	Min [K]	Max [K]
23.8	0.30	0.91	0.48	1.19
31.4	0.31	0.82	0.70	1.90
72.5	1.22	5.57	3.05	11.34
82.5	1.62	8.97	4.34	16.33

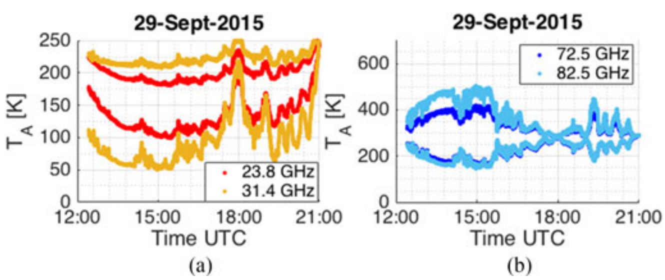

Fig. 4. Time series of ST-MWR measurements in terms of antenna noise temperatures for a case studies in presence of clouds or precipitation (29 September 2015) at the four AFRL-MWR available frequencies. (a) 23.8 and 31.4 GHz. (b) 72.5 and 85.5 GHz.

respect to the results at 20.7 GHz in [25] and [26], we have obtained percentage deviations of 14.2% and 20.9%, respectively; 2) comparing the result at 31.4 GHz in Table III with respect to the results at the same frequency in [25] and [26], we have obtained percentage deviations of 4.0% and 11.7%, respectively. It is pointed out here that in the ST technique, at frequencies above 10 GHz, the Sun appears as a rather uniform disk [3] and the solar activity in our observations has little effect due to a large field of view of the radiometer antenna main-beam. Therefore, the Sun can be considered as a constant source in our application, apart from multiyear solar cycles.

V. EXTINCTION ESTIMATES IN PRECIPITATING CLOUDS

Sun brightness temperatures have been set to fixed values according to Table III, in particular the Langley results have been taken into account during the following analysis.

Fig. 4 shows the time series of the ST-MWR measurements of both *ooS* (lower curves) and *twS* (upper curves) antenna noise temperatures for the case study of September 29, 2015 at the four AFRL-MWR available frequencies. With respect to the clear-sky case shown in Fig. 1, it is shown how in the presence of clouds or precipitation, the brightness temperature difference between the two measurement modes *ooS* and *twS* decreases when the atmospheric extinction significantly increases, this behavior being more dominant at V and W band than at K and Ka band. Indeed, the *ooS* brightness temperature increases because of the contributing emission from clouds and precipitation while correspondingly the Sun signal is attenuated in the *twS* brightness temperature. The decrease in T_A is clearly evident at V- and W-band, where the Sun provides the larger contribution. Conversely at K band, where the atmosphere signal is also providing a strong contribution, the *twS* noise temperatures also increases, although with less impact.

The ST-MWR technique is able to estimate a valid atmospheric extinction, according to (22), only if consistent antenna noise temperature differences are available. During intense rain events ΔT_A differences can reach zero or even negative, which limits the application of this technique. The maximum atmospheric extinction value $A_{\mathrm{ST\ max}}$ depends on both considered frequency and std $\mathrm{std}(\Delta T_A)$ and it can be computed from (22). By considering a measurement deviation equal to the MW radiometric brightness temperature absolute accuracy (equal to 0.5 K at K-band and 1 K at W-band), we can evaluate the std of the noise temperature difference from (10) according to:

$$\mathrm{std}\left(\Delta T_A\right) = \sqrt{\mathrm{var}\left(T_{A\mathrm{ooS}}\right) + \mathrm{var}\left(T_{A\mathrm{twS}}\right)} \qquad (27)$$

where "var" stands for the noise variance equal to the square of the absolute accuracy. By properly substituting $\mathrm{std}(\Delta T_A)$ values (0.7 at K and Ka band and 1.4 at V W band) in (22), the maximum atmospheric extinction values result about 22 dB, 24 dB, 26 dB and 27 dB, at 23.8, 31.4, 72.5 and 82.5 GHz, respectively. The percentages of ΔT_A values lower than its std result less than 0.1% at K and Ka band and 0.6% at V and W band, taking into account the entire available dataset described in Section III.

As described in [4] and [13], the ST-MWR technique can offer a very interesting framework to validate parametric retrieval models, especially at frequency bands above K band due to the unavailability of satellite-to-Earth beacon campaigns. Previous works already proposed physically-based prediction models (PPM) for estimating atmospheric parameters based on the nonlinear regression fit of numerical simulations [17], [36]. Sky-noise Eddington radiative transfer model (SNEM) has been considered in an absorbing and scattering medium such as gaseous, cloudy, and rainy atmosphere [37], [31]. The exploitation of the closest RaOb dataset has been used to statistically characterize the local meteorology in terms of temperature, pressure, and humidity average and standard-deviation profiles. The latter statistics is then imposed in the Monte Carlo pseudo-random generation of vertical cloud structures where average profiles and cross correlation among hydrometeor concentration are imposed [36], [37].

The PPM general approach has been adapted for Rome (NY, USA) using our available radiosonde dataset described in Section III-B and performing SNEM simulations at 23.8, 31.4, 72.5, and 82.5 GHz and for eight elevation angles between 20° and 90° in in terms of both brightness temperature and atmospheric extinction.

The multifrequency PPM-*PolDEx* model [4] is based on a polynomial regression on SNEM dataset, reinforced with a double exponential single-frequency term, able to achieve better results in heavier rainy cases. This multifrequency weighted approach polynomial is able to balance the use of two different models depending on the weather conditions. The PPM-*PolDEx*

This article has been accepted for inclusion in a future issue of this journal. Content is final as presented, with the exception of pagination.

TABLE V
ATMOSPHERIC EXTINCTION INTERCOMPARISON BETWEEN ST-MWR AND PPM-POLDEX MODEL FOR THE AVAILABLE DATASET IN 2015 IN ROME, NY, USA ALL-WEATHER CASES

f [GHz]	AvE[dB]	RMSE[dB]	CC	IA
23.8	0.0069	0.1721	0.9800	0.9893
31.4	–0.0500	0.2441	0.9846	0.9860
72.5	0.0593	0.7061	0.9791	0.9793
82.5	0.0513	0.6242	0.9808	0.9861

atmospheric extinction estimates are given by:

$$A_{\mathrm{Pol}DEx}(f) = m\left\{\left(1 - \mathrm{SSI} + h\right) A_{\mathrm{Pol}}(f) + (\mathrm{SSI} - h)\, A_{DEx}(f)\right\} \qquad (28)$$

where

$$A_{\mathrm{Pol}}(f) = \sum_{i=1}^{4} a_i\, T_{A\mathrm{ooS}}(f_i) + b_i\, T^2_{A\mathrm{ooS}}(f_i) \qquad (29)$$

$$A_{DEx}(f) = \left[c_1 e^{c_2 T_{A\mathrm{ooS}}(f)} + d_1 e^{d_2 T_{A\mathrm{ooS}}(f)}\right] \qquad (30)$$

where $f_{i=1,2,3,4} = 23.8, 31.4, 72.5, 82.5$ GHz and f is one of four available frequencies f_i, whereas the coefficients are all function of the air mass *m.* A first comparison is here performed among all-weather conditions available from the six months of measurements. Table V quantifies the comparison in terms of average error (AvE) and root-mean-square-error (RMSE), with the error defined as the difference between the PPM model and the ST time series. We can clearly note how the PPM-*PolDEx* parametric model shows solid results at all frequencies and for the entire range of elevation angles. In order to stress the last consideration, the correlation coefficient (CC) and the index of agreement (IA) have been also considered to better evaluate the percentage accuracy. IA is a standardized measure of the degree of model prediction error and it varies between 0 and 1. An agreement index score of 0 suggests no agreement between the PPM model and the SNEM dataset, while an agreement score of 1 suggests complete match between the model and the dataset [38]. For the PPM-*PolDEx* model in Table V, IA goes from about 0.99 at 23.8 GHz to about 0.98 at 72.5 GHz.

Measurements, described in Section III, are available at different elevation angles since the ST technique is intrinsically based on a variable antenna pointing in order to follow the Sun movement along its ecliptic. Both ST and PPM-*PolDEx* estimates are able to provide valid results for a wide range of elevation angles. In particular, the measurements result equally distributed with about 33.9% between 70° and 54°, 43.1% between 53° and 38° and 22.5% between 37° and 20° in elevation.

In order to focus the emphasis on cloudy and rainy conditions, the threshold criterion described in Section III-A has been used to define the total percentage of clear-air samples (30.5%), as well as the one of cloudy/rainy situations (69.5%).

Fig. 5(a)–(d) shows the scatterplot of *PPM-PolDEx* model atmospheric extinction estimates for each frequency versus the corresponding ST-MWR ones for all the available dataset for only cloudy/rainy situations. A saturation effect is shown in the ST extinction retrieval, especially at V and W-band, attesting the limits of the ST technique in terms of the maximum attainable extinction. It generally occurs for heavy rain at K-band, but it may occur for light rain at 72.5 and 82.5 GHz. In such conditions antenna noise temperature differences ΔT_A between *twS* and *ooS* are minimal and can reach the noise level.

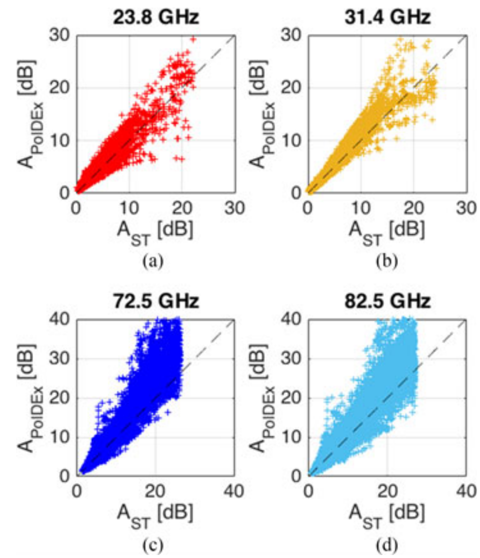

Fig. 5. Scatterplot of ST-MWR atmospheric extinction for each frequency versus extinction estimates from PPM-PolDEx for all cloudy/rainy conditions.

TABLE VI
ATMOSPHERIC EXTINCTION INTERCOMPARISON BETWEEN ST-MWR AND PPM-POLDEX MODEL FOR THE AVAILABLE DATASET IN 2015 IN ROME, NY CLOUDY AND RAINY CASES

f [GHz]	AvE[dB]	RMSE[dB]	CC	IA
23.8	0.0093	0.2014	0.9778	0.9881
31.4	–0.0315	0.2820	0.9848	0.9864
72.5	0.0933	0.8421	0.9790	0.9780
82.5	0.0893	0.7425	0.9796	0.9849

Table VI quantifies the comparison in terms of AvE and RMSE, CC, and the IA. Both scatterplots and numerical results confirm that the exclusion of the clear-air samples in the comparison has a minimum impact on the comparison and the *PolDEx* approach shows a good correlation with respect to ST data for all frequencies in cloudy/rainy situations.

VI. CONCLUSION

Two possible applications of STmicrowave radiometry have been explored in this paper. The ST technique has been introduced to estimate the Sun brightness temperature at K, Ka, V, and W band. In the Appendix, a detailed theoretical framework has been proposed to evaluate the overall error budget with respect to several uncertainties due to radiative parameters, spectral response, actual antenna patterns and beam filling factor. This approach has clearly identified the critical assumptions behind the ST-MW radiometric data processing such as the precision of the pointing at the Sun with the change in elevation, the atmospheric stationarity within each ST switch,

This article has been accepted for inclusion in a future issue of this journal. Content is final as presented, with the exception of pagination.

as well as the accurate knowledge of the antenna characteristics, which is the most significant factor affecting the estimation accuracy.

Two methods have been applied, the elevation-scanning Langley method and surface meteorological data method. The two techniques showed comparable results, but the first one need a careful selection of candidate clear-air days whereas the second one is depending on the external weather station data. Both techniques are affected by the daily variability of clear air extinction. The use of the two methods allowed us to give an uncertainty indication related to different adopted techniques. Since ST measurements are currently still being collected, it is intriguing to speculate the possibility of observing solar cycles in the retrieved Sun brightness temperature, although such variability is partly masked by the intrinsic accuracy of the estimates.

ST-MWR has been also applied to estimate the atmospheric path attenuation in all-weather conditions at K, Ka, V, and W band. In the presence of precipitating clouds, the technique allowed the estimate of the atmospheric extinction of about 25 dB at K-band and up to about 30 dB at V- and W-band. The method has been applied, as a source of validation, for estimating the accuracy of the multifrequency PPM-*PolDEx* model, showing a very good agreement with the ST retrievals in cloudy and rainy conditions, with an rms agreement of about 0.2 dB at K-band and 0.7 dB at V-band.

With the availability of a larger dataset of measurements, the ST-MWR technique will be useful in further developing the physically-oriented parametric models. In particular, open issues are related to the analysis of cloudy and rainy events at low elevation angles, where prediction models generally have large errors, as well to the discrimination between heavy clouds and light rain. In case of precipitation, ST-MWR can be also use to assess the capability of MWR to estimate rainfall rate and to relate the latter to atmospheric path attenuation. Finally, a longer time series of Sun brightness temperature estimates can provide a better confidence of the performed estimates using ground-based ST-MWR.

Appendix
Error Sensitivity Analysis

The sensitivity analysis of sun brightness temperature estimate to residual errors or uncertainties of ST-MWR measurements is fundamental to understand the expected accuracy of the technique. The following Section A of this Appendix is devoted to this analysis. Further considerations are also provided in the next Sections B and C where the impact of the instrument spectral response and the radiometer antenna side lobes is discussed, respectively.

A. *Theoretical Analysis of Error Sources*

Several sources of uncertainty in ST-MW radiometry can be identified: 1) different adopted techniques; 2) beam filling factor; 3) antenna pattern; 4) elevation scanning. In order to perform this error budget analysis, we can use the first-order

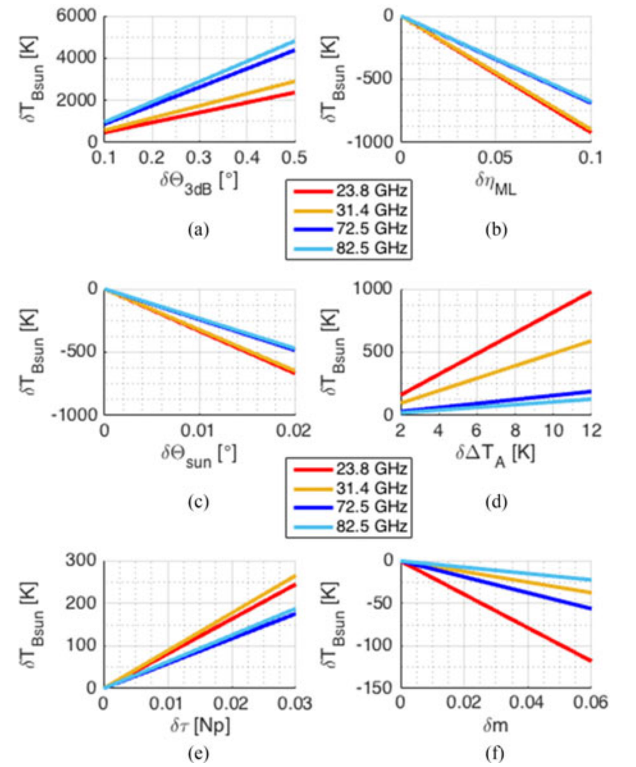

Fig. 6. Sensitivity analysis of ST-MWR performances for a set of values which are those expected between Ka and W band.

error propagation theory by assuming a statistical independence among the error sources.

Primarily, uncertainties of the beam-filling factor f_Ω have to be considered to evaluate its impact in the $T_{B\ \mathrm{sun}}$ estimation, considering that $T_{B\ \mathrm{sun}} = T^*_{B\ \mathrm{sun}}/f_\Omega$. In a general way, these are related to errors associated to the Sun radiation solid angle $\Omega_{\mathrm{P\ sun}}$ and the antenna radiation solid angle Ω_{Pant}. Starting from (7), the uncertainty in $T_{B\ \mathrm{sun}}$ because of variation in $\Omega_{\mathrm{P\ sun}}$ is given by $\delta T_{B\ \mathrm{sun}} = (T^*_{B\ \mathrm{sun}}/\Omega_{\mathrm{P\ sun}})\delta\Omega_{\mathrm{Pant}}$, where the variations in Ω_{Pant} are mainly due to the knowledge of the antenna radiation pattern and the half-power beamwidth values. Analogously, $T_{B\ \mathrm{sun}}$ uncertainty because of variations in $\Omega_{\mathrm{P\ sun}}$ can be obtained from (7) leading to $\delta T_{B\ \mathrm{sun}} = -T^*_{B\ \mathrm{sun}}(\Omega_{\mathrm{Pant}}/\Omega^2_{\mathrm{P\ sun}})\ \delta\Omega_{\mathrm{P\ sun}}$ and variations in $\Omega_{\mathrm{P\ sun}}$ shall be computed considering the simplified expression in (17) or the general expression for a Gaussian beam in (19). The latter depends on both the Sun disk diameter and half-power beamwidth values. For this reason, a more general sensitivity analysis can be achieved from (21) considering $\delta T_{B\ \mathrm{sun}}$ because of variation in Θ_{ML}, which yields the following uncertainty:

$$\delta T_{B\ \mathrm{sun}} = \frac{2\ln(2)\ \eta_{\mathrm{ML}}\ T^*_{B\ \mathrm{sun}}}{f^2_\Omega} \frac{\Theta^2_{\mathrm{sun}}}{\Theta^3_{\mathrm{ML}}} e^{-\ln(2)\left(\frac{\Theta_{\mathrm{sun}}}{\Theta_{\mathrm{ML}}}\right)^2} \delta\Theta_{\mathrm{ML}}. \tag{A.1}$$

Fig. 6(a) shows the previous expression using the AFRL half-power beamwidth values and the Sun zenithal plane angle described in Section III-D and using $T^*_{B\ \mathrm{sun}}$ values in Table IV. It can be noted that the uncertainty in the value of Θ_{ML} provides a large source of error for the estimate of $T_{B\ \mathrm{sun}}$. For an uncertainty of Θ_{ML} up to $0.3°$, the error in estimating $T_{B\ \mathrm{sun}}$

TABLE VII
EXPECTED ERRORS IN $T_{B\,\mathrm{sun}}$ DUE TO FILLING FACTOR VARIATIONS

	$\delta T_{B\ \mathrm{sun}}$ versus $\delta\Theta_{\mathrm{ML}}$		$\delta T_{B\ \mathrm{sun}}$ versus $\delta\Theta_{\mathrm{sun}}$	
f [GHz]	$\delta\Theta_{\mathrm{ML}}$ [°]	$\delta T_{B\ \mathrm{sun}}$ [K]	$\delta\Theta_{\mathrm{sun}}$ [°]	$\delta T_{B\ \mathrm{sun}}$ [K]
23.8	0.41	1946	0.0019	–63.3
31.4	0.33	1915	0.0030	–97.0
72.5	0.17	1489	0.0119	–287.5
82.5	0.14	1348	0.0152	–356.9

TABLE VIII
EXPECTED ERRORS IN $T_{B\ \mathrm{sun}}$ DUE TO RADIATING QUANTITY VARIATIONS

	$\delta T_{B\ \mathrm{sun}}$ versus $\delta\Delta T_A$		$\delta T_{B\ \mathrm{sun}}$ versus $\delta\tau$	
f [GHz]	$\delta\Delta T_A$ [K]	$\delta T_{B\ \mathrm{sun}}$ [K]	$\delta\tau$ [Np]	$\delta T_{B\ \mathrm{sun}}$ [K]
23.8	4	326	0.019	155
31.4	5	245	0.009	79
72.5	8	126	0.015	87
82.5	10	108	0.021	131

goes from 1424 K at Ka band up to 2888 K at W band. In a more quantitative way, $\delta T_{B\ \mathrm{sun}}$ has been be evaluated from (A.1) considering a difference of 11% in Θ_{ML} (worst case at 31.4 and 72.5, as the differences among AFRL values described in Section III-D and RPG LPW-U72-82 Θ_{ML} values from manufacturer specification). The results are given in Table VII (left side). Furthermore, starting from (21), errors in $T_{B\ \mathrm{sun}}$ due to main beam efficiency η_{ML} variation have to be taken into account according to:

$$\delta T_{B\ \mathrm{sun}} = -\frac{T^*_{B\ \mathrm{sun}}}{\eta_{\mathrm{ML}} f_\Omega}\delta\eta_{\mathrm{ML}}. \quad \text{(A.2)}$$

Fig. 6(b) shows the previous expression using values of interest in Table IV and η_{ML} described in Section III-D. For an uncertainty of η_{ML} up to 0.05, $\delta T_{B\ \mathrm{sun}}$ goes from –330 K at W band up to –450 K at Ka band. Error sources in both (A.1) and (A.2) imply that the AFRL-MWR antenna pattern should be known with a high degree of accuracy.

Analogously, the uncertainty in $T_{B\ \mathrm{sun}}$, because of variations in Θ_{sun}, can be computed from (21) yielding the following uncertainty:

$$\delta T_{B\ \mathrm{sun}} = \frac{-2\ln(2)\ \eta_{\mathrm{ML}}\ T^*_{B\ \mathrm{sun}}}{f_\Omega^2}\frac{\Theta_{\mathrm{sun}}}{\Theta^2_{\mathrm{ML}}} e^{-\ln(2)\left(\frac{\Theta_{\mathrm{sun}}}{\Theta_{\mathrm{ML}}}\right)^2}\delta\Theta_{\mathrm{sun}}. \quad \text{(A.3)}$$

Since the Earth–Sun distance changes over the year, the disk angle subtended by the Sun varies between 0.526° and 0.545°. This leads to a maximum Θ_{sun} variation of 0.019°.

Fig. 6(c) shows (A.3) using the same values of the previous analyses, for Θ_{sun} variations of about 0.01° (maximum deviation from the value reported in Section III-D), the error in estimating $T_{B\,\mathrm{sun}}$ is relatively small and it goes from –240 K at 82.5 GHz up to –340 K at 23.8 GHz. Table VII (right side) reports the uncertainty in $T_{B\,\mathrm{sun}}$ because of Θ_{sun} variations in more detail, considering $\delta\Theta_{\mathrm{sun}}$ values obtained by calculating the difference between the general formulation in (19) and the approximation in (17). This approximation leads to small errors in $T_{B\ \mathrm{sun}}$ with respect to previous sources, especially at lower frequencies where the effect of the radiometer antenna pattern can be neglected in (16). Second, error analyses with respect to radiating quantities have to be carried out. Sensitivity $\delta T_{B\ \mathrm{sun}}$ with respect to $\delta\Delta T_A$ is obtained from the governing (11) and (15) of ST-MWR leading to:

$$\delta T_{B\ \mathrm{sun}} = \frac{1}{f_\Omega} e^{\tau}\ \delta\Delta T_A. \quad \text{(A.4)}$$

Fig. 6(d) shows the sensitivity to ΔT_A, in which τ values expected in clear-sky situations between K and W band were used ($\tau = 0.10$, 0.05, 0.30, and 0.15 Np for the four available frequencies, respectively). Since ΔT_A values are much smaller at K band with respect to V band, $\delta\Delta T_A$ uncertainties have larger effects at lower frequencies with respect to higher frequencies. Uncertainties are due to calibration errors and antenna mispointing during ST and atmospheric variability. The first is estimated to be less than 0.5 K at K and Ka band and about 1 K at W and V-band, whereas the latter goes from 4 K to 10 K with increasing frequency, whose reduction has suggested the filtering approach used in Section III-C. For an uncertainty in ΔT_A of about 8 K, the error in $T_{B\ \mathrm{sun}}$ goes from 86 K at 82.5 GHz up to 652 K at 23.8 GHz. Quantitative analysis of (34) is reported in the left side of Table VIII, considering $T_{B\ \mathrm{sun}}$ uncertainties for typical ΔT_A in clear air. The latters have been derived from the variability of AFRL-MWR data during the *ooS* and *twS* switching. In this case, $\delta T_{B\ \mathrm{sun}}$ are less than 4% at all frequencies with respect to the absolute values (worst case at 23.8 GHz).

Furthermore, we can obtain the uncertainty in $T_{B\ \mathrm{sun}}$ due to atmospheric extinction variations $\delta\tau$ from the same equations as before:

$$\delta T_{B\ \mathrm{sun}} = \frac{1}{f_\Omega}\ \Delta T_A\ e^{\tau}\ \delta\tau. \quad \text{(A.5)}$$

Fig. 6(e) shows the relation for the same set of τ values and for ΔT_A values expected in clear-sky situations ($\Delta T_A = 100$, 180, 370, and 580 K for the four available frequencies, respectively). For an uncertainty in τ of about 0.02 Np, the error in $T_{B\ \mathrm{sun}}$ goes from 117 K at 72.5 GHz up to 176 K at 31.4 GHz. The two considered techniques use different methods to evaluate the atmospheric extinction: 1) Langley technique estimates τ_z through the slope of the linear regression in (13), representing a daily average atmospheric extinction (the associated error is mainly due to the attenuation variability during the day and ST antenna mispointing); 2) Meteorological technique needs an estimate of τ to be computed according to (14). This means that both mean radiating temperature and antenna noise temperature *ooS* errors have to be taken into account. Note that for the meteorological technique we can provide a daily averaged value of Sun brightness temperature in order to mitigate the punctual $T_{B\ \mathrm{sun}}$ uncertainties due to $\delta\tau$. Starting from (14), the uncertainty in τ because of variation in $T_{A\mathrm{ooS}}$ is given by:

$$\delta\tau = -\frac{\delta T_{A\mathrm{ooS}}}{(T_{\mathrm{mr}} - T_{A\mathrm{ooS}})} \quad \text{(A.6)}$$

Considering a fixed mean radiating temperature of 270 K and typical $T_{A\mathrm{ooS}}$ values expected in clear-air situations ($T_{A\mathrm{ooS}} =$ 35, 20, 100, and 60 K for the four available frequencies, respectively), we can estimate $\delta\tau$ associated to the $\delta T_{A\mathrm{ooS}}$ absolute accuracies (equal to 0.5 K at K-band and 1 K at W-band according to the manufacturer specifications). Resulting $\delta\tau$ values are relatively small and they go from –0.0021 Np at 23.8 GHz up to –0.0059 Np at 72.5 GHz.

Furthermore, $\delta\tau$ uncertainty due to errors in estimating T_{mr} leads to:

$$\delta\tau = \frac{T_{\cos} - T_{A\mathrm{ooS}}}{(T_{\mathrm{mr}} - T_{\cos})\ (T_{\mathrm{mr}} - T_{A\mathrm{ooS}})}\,\delta T_{\mathrm{mr}}. \tag{A.7}$$

Since $T_{A\mathrm{ooS}}$ assumes smaller values at K band with respect to V band, $\delta\tau$ uncertainties have larger effects at higher frequencies. This behavior is the opposite of what happens in (A.5), where $\delta T_{B\ \mathrm{sun}}$ grows with decreasing frequency. For an uncertainty in T_{mr} of 3 K, the error in τ goes from –0.0008 Np at 31.4 GHz up to –0.006 Np at 72.5 GHz, using the same clear-air values of the previous analysis.

On the right side of Table VIII, the error budget analysis of $T_{B\ \mathrm{sun}}$ is shown with respect to uncertainties $\delta\tau$. The latter have been derived from both τ_z confidence intervals of the linear regression slope in (13) and the std of the estimated atmospheric extinction time series in (14). The resulting values are very similar for both techniques. Errors in Sun brightness temperature are less than 2% at all frequencies with respect to the absolute values (worst case at 82.5 GHz).

Further error should be considered whether different elevation angles are assumed between off-the-Sun and twS observations in the computation of the antenna noise temperature difference. Considering an *ooS* observation in (9) performed at an elevation angle θ_1, the antenna noise temperature difference in (10) depends on both elevation angles (or air-masses). The $T_{B\ \mathrm{sun}}$ uncertainty due to the air mass variation δm between the two observations is given by:

$$\delta T_{B\ \mathrm{sun}} = \frac{(T_{\cos} - T_{\mathrm{mr}})\ \ \tau}{f_\Omega}\,\delta m. \tag{A.8}$$

Note that the atmospheric transmittance ratio has been truncated to the first order the Taylor expansion. Fig. 6(f) shows the previous equation for the same set of values used before for the four AFRL-MWR frequencies. For an air-mass uncertainty of about 0.4 (worst case corresponding to a variation of about 3° from the minimum admitted elevation angle of 20°), the error in estimating $T_{B\ \mathrm{sun}}$ increases with the frequency decrease and goes from –14 K up to –79 K.

Finally, we estimated the error in assuming the horizontal homogeneity in clear sky through the analysis of the estimated atmospheric extinction time series in (14) at the same elevation and different azimuths. Uncertainties of τ were estimated as 0.0039, 0.0016, 0.0053, and 0.0062 Np for an average azimuth distance of 5 deg. As such, the assumption holds.

B. Impact of Radiometer Spectral Response

Radiometer characteristics, such as antenna pattern and receiver bandwidth, are relevant aspects to be considered when dealing with the development of algorithms, intercomparisons with radiative transfer model simulations and data assimilation [39]. In order to rigorously approach these issues, the expression in (1) needs to be generalized to include the dependency on frequency so that the band-averaged antenna noise temperature is given by:

$$T_A(\theta_0, \varphi_0) = \int_B \frac{\int_{4\pi} T_{Bf}(\theta, \varphi, f)\, F_{nf}(\theta_0, \varphi_0, \theta, \varphi, f)\, d\Omega}{\int_{4\pi} F_{nf}(\theta_0, \varphi_0, \theta, \varphi, f)\, d\Omega} \times\ H_n(f)\,\mathrm{d}f \tag{A.9}$$

where H_{n} is the normalized spectral response function (SRF) of the instrument within the bandwidth *B* so that

$$\int_B H_n(f)\, df = 1. \tag{A.10}$$

The band-averaged T_A in (A.9) is now expressed, with respect to (1), as the filtering of the spectral brightness temperature T_{Bf} through the instrumental SRF within the frequency bandwidth *B*. Moreover, in (A.9) the antenna power radiation pattern F_{nf} is also dependent on frequency.

Generally speaking, instrument narrow bandwidths allow us to apply the approximation that spectral functions T_{Bf}, F_{nf}, and H_n can be considered constant over *B* so that (A.9) reduces to (1). The impact of such approximation in our model development is analyzed in this section. Note that the frequency dependence of F_{nf} can be usually neglected without loss of accuracy for the window frequencies, but for high-frequency double-sideband channels around the absorption peak frequencies, it may not be negligible and F_{nf} should be possibly measured for the low and high sidebands.

In our work we should consider that AFRL-MWR channels at K-band at 23.8, 31.4 center frequency have relatively narrow bandwidths of 230 MHz, but the V- and W-band channels at 72.5 and 82.5 GHz have a bandwidth as large as 2 GHz. As recognized in [39], the errors associated to receiver channel bandwidth are less important in K-band and W-band, but this is not necessarily true for channels in the V-band or higher frequencies in the wings of absorption lines. On the one hand, highly asymmetric SRF can change the effective frequency of a radiometric channel, whereas on the other hand, spectral brightness temperature T_{Bf} due to the atmosphere can significantly vary within the same bandwidth *B* [40], [41].

Regarding the SRF characterization of AFRL-MWR, the receivers are tuned by the manufacturer as a complete system so that the radiometer channel central frequency is a good representation of the filter response [23], [28]. For filter tuning a calibrated monochromatic input signal is swept over the spectrum, the digital radiometer output is monitored and the effective central frequency calculated. This implies that in our case the use of the effective central frequency is a good approximation for our purposes, provided that actual SRFs were not available from the manufacturer.

Indeed, the spectral variability of T_{Bf} within the assigned bandwidth *B* needs to be quantified to estimate the error due to monochromatic approximation at effective central frequency. To examine the SRF impact, we have simulated monochromatic brightness temperatures T_{Bf} in (A.9) with steps of 200 MHz at V and W band and performed several band-averaging summing them according to specific weights. We have modeled the SRF weights H_{n} in (A.9) in order to reproduce the shapes of realistic asymmetric spectral response functions, similar to those found in literature (e.g., as in [42]). Differences between monochromatic and band-averaged simulations can be up to 1.5 K at 72 GHz and 0.1 K at 82.5 GHz. As previously stated, this result is expected being the spectral variability more relevant for the 72.5 GHz channel as it is closer to the oxygen absorption wing. According to our evaluations, it is highly advisable that the radiometer characteristics, such as SRF and antenna patterns, are made available to users, especially in future applications at millimetre-wave frequency channels, as recommended in [41].

C. Impact of Radiometer Antenna Side Lobes

As described in Section II, the approximation of an antenna Gaussian beam has been used for computing f_Ω. Provided that actual antenna patterns of AFRL-MWR were not available from the manufacturer, the Gaussian shape antenna proposed here has been favored with respect to other possible approximations, such as a pattern described by Bessel functions, since: 1) the main lobe of AFRL-MWR is well characterized by the Gaussian shape, as suggested by the manufacturer [23], [28]; 2) the side-lobe levels produced by the feedhorn/parabola system are below –30 dB at 23.8 and 31.4 GHz and below –40 dB at 72.5 and 82.5 GHz [23]. This limits the use of Bessel functions which generally provide higher side lobes unless additional tapering by other functions is introduced.

The antenna radiation pattern is, however, characterized not only by the main lobe. In this section the effect of neglecting antenna pattern side lobes is evaluated. In our retrievals and in clear sky conditions, the effect of side lobes may be relevant: 1) at very low elevations when side lobes can pick up ground radiation (but typically the radiometer is not operated below 10°); 2) during the switch when the Sun can be picked up by the side lobes (at least the first one) when observing in the “off the sun” mode.

In order to take into account the side lobe contributions and to evaluate them quantitatively, a Gaussian-shape has been also employed to model both the main lobe and the side lobes centered in $\theta_{i=1,\ldots,m}$ in the radiometer antenna normalized pattern F_n

$$F_n(\theta,\varphi) = F_{n\mathrm{ML}}(\theta,\varphi) + \sum_{i=1}^{m} F_{n\mathrm{SL}i}(\theta,\varphi) = e^{-\ln(2)\left(2\frac{\theta}{\Theta_{\mathrm{ML}}}\right)^2} + \sum_{i=1}^{m} A_i\, e^{-\ln(2)\left(2\frac{\theta-\theta_i}{\Theta_{\mathrm{SL}i}}\right)^2} \quad \text{(A.11)}$$

considering *m* side lobes in the general expression above, θ_i, φ_i as the side lobe pointing angles and Θ_{ML} and $\Theta_{\mathrm{SL}i=1,\ldots,m}$ as the half-power beamwidth values for the main lobe and the side lobes, respectively. In (A.11), it is reasonable to assume negligible the tails of the Gaussian pattern shapes outside of each respective beam, with an impact generally less than 0.1%.

The antenna radiation-pattern solid angle Ω_{Pant} can be obtained from (2) using (A.11):

$$\Omega_{\mathrm{Pant}} = \Omega_{\mathrm{PML}} + \sum_{i=1}^{m} \Omega_{\mathrm{PSL}i} \quad \text{(A.12)}$$

where Ω_{PML} and $\Omega_{\mathrm{PSL}i}$ stand for antenna main lobe radiation-pattern solid angle and the antenna side lobe radiation-pattern solid angles, respectively. By properly evaluating the integrals, the following expressions have been obtained for the aforementioned antenna radiation-pattern solid angles:

$$\Omega_{\mathrm{PML}} \cong \frac{\pi}{4\ln(2)}\Theta_{\mathrm{ML}}^2\left[1 - e^{-\ln(2)\left(\frac{2\pi}{\Theta_{\mathrm{ML}}}\right)^2}\right] \quad \text{(A.13)}$$

$$\Omega_{\mathrm{PSL}i} \cong 2\pi A_i \left\{\frac{\Theta_{\mathrm{SL}i}^2}{8\ln(2)}\left(e^{-a_i^2} - e^{-b_i^2}\right) + \frac{\sqrt{\pi}\,\Theta_{\mathrm{SL}i}\theta_i}{4\sqrt{\ln(2)}}\left[\mathrm{erf}(b_i) - \mathrm{erf}(a_i)\right]\right\} \quad \text{(A.14)}$$

where

$$a_i = \frac{2\sqrt{\ln(2)}}{\Theta_{\mathrm{SL}i}}\theta_i\,; \quad b_i = \frac{2\sqrt{\ln(2)}}{\Theta_{\mathrm{SL}i}}(\pi + \theta_i)\,. \quad \text{(A.15)}$$

As described in [24], corrugated feedhorns have traditionally used a linearly tapered internal profile with main-beam efficiencies even greater than 98%. By including the parabola spillover, we can estimate an overall main-lobe efficiency by means of

$$\eta_{\mathrm{ML}} = \eta_s\eta'_{\mathrm{ML}} = \eta_s\frac{\Omega_{\mathrm{PML}}}{\Omega_{\mathrm{Pant}}} \quad \text{(A.16)}$$

where η_{ML} is the overall efficiency, η_s is the spillover efficiency, and η'_{ML} is the feedhorn main lobe efficiency. By properly evaluating (A.12) and (A.13) we can retrieve a reasonable value of $\eta'_{\mathrm{ML}} = \Omega_{\mathrm{PML}}/\Omega_{\mathrm{Pant}}$ for each considered frequency. In the radiometer antenna normalized pattern F_n, we have considered equally spaced side lobes with constant half-power beamwidth values $\Theta_{\mathrm{SL}i}$, equal to $\Theta_{\mathrm{ML}}/2$. Furthermore, in order to have an upper boundary condition, we have assumed that the 99.9% of the total power is received within 30° from the pointing angle of the main lobe. The values of A_i have been set to –30 dB (10^{-3}) at 23.8 and 31.4 GHz and to –40 dB (10^{-4}) at 72.5 and 82.5 GHz, according to [23]. Considering spillover efficiencies η_s of 0.98 at Ka band and 0.99 at V–W bands, we have obtained η_{ML} values equal to 0.969, 0.969, 0.979, and 0.979 at 23.8, 31.4, 72.5, and 82.5 GHz, respectively. The effect on $T_{B\mathrm{sun}}$ estimates due to uncertainty in η_{ML} is also analyzed in (A.2) [see Fig. 6(b)]. By considering the side lobe contributions in (1), we obtain

$$\begin{aligned} T_A(\theta_0,\varphi_0) &= \eta_s\frac{\Omega_{\mathrm{PML}}}{\Omega_{\mathrm{Pant}}}T_{B\mathrm{ML}}(\theta_0,\varphi_0) + \eta_s\frac{\sum_{i=1}^{m}\Omega_{\mathrm{PSL}i}T_{B\mathrm{SL}_i}(\theta_i,\varphi_i)}{\Omega_{\mathrm{Pant}}} + (1-\eta_s)\,T_{B\,\mathrm{Spill}} \\ &= \eta_s\eta'_{\mathrm{ML}}T_{B\mathrm{ML}}(\theta_0,\varphi_0) + \eta_s(1-\eta'_{\mathrm{ML}})\overline{T_{B\mathrm{SL}}} + (1-\eta_s)\,T_{B\,\mathrm{Spill}} \end{aligned} \quad \text{(A.17)}$$

where θ_i, φ_i represent the pointing angles of the side lobes, $\overline{T_{B\mathrm{SL}}}$ is the averaged contribution of side lobes and $T_{B\,\mathrm{Spill}}$ is the spillover brightness contribution. By supposing $T_{B\ \mathrm{Spill}} \cong \overline{T_{B\mathrm{SL}}}$, we can retrieve from (A.17) the deviation δT_A due to side lobe and spillover effects

$$\begin{aligned}\delta T_A &= \eta_s\,(1-\eta'_{\mathrm{ML}})\,\overline{T_{B\mathrm{SL}}} + (1-\eta_s)\,T_{B\ \mathrm{Spill}}\\ &\cong\ (1-\eta_{\mathrm{ML}})\ \overline{T_{B\mathrm{SL}}}.\end{aligned} \tag{A.18}$$

Referring to (A.17), the impact of an additive side lobe radiation is negligible in (6) since, when the main lobe is pointing toward the sun $T_{B\mathrm{ML}} = T_{B\mathrm{twS}}$, all the side lobes are pointing toward the same clear-air scenario $\overline{T_{B\mathrm{SL}}}\ \cong T_{B\mathrm{ooS}}$. This condition gives brightness contributions from 20 K at 31.4 GHz up to 100 K at 72.5 GHz, corresponding to $\delta T_{A\mathrm{twS}}$ going from 0.6 K to 2 K. Considering the same analysis carried out for (5), we have to take into account the possibility that, during the switch, the Sun can be picked up by one of the side lobes when observing "off the Sun", i.e., the contribution of the side lobes is not uniform. We can rewrite (A.18) as

$$\delta T_A = (1-\eta_{\mathrm{ML}})\left[w_{\mathrm{SL}}\ T_{B\mathrm{twS}} + (1-w_{\mathrm{SL}}\ )\ \overline{T_{B\mathrm{SL}}}\ \right] \tag{A.19}$$

where w_{SL} is the weight of the side lobe picking up the Sun radiation. To evaluate a worst-case scenario, we have supposed to have the Sun precisely centered by the first side lobe that contributes for the 80% ($w_{\mathrm{SL}}\ = 0.8$) with respect to the other side lobes. Using typical clear-air $T_{B\mathrm{twS}}$ values from 150 K at 23.8 GHz to 600 K at 82.5 GHz, we can obtain $\delta T_{A\mathrm{ooS}}$ values going from 4 K to 10 K. These values of δT_A lead to ΔT_A errors that affect the $T_{B\ \mathrm{sun}}$ estimates as discussed in detail in (A.4) of this Appendix.

Acknowledgment

The authors would like to thank Prof. P. Ciotti (University of L'Aquila) and Prof. P. Basili (University of Perugia) for their insights in the development of the PPM-*PolDEx* model. The work of L. Milani was carried out within the Excellence program and a *post-lauream* contract with the Sapienza University of Rome, Rome, Italy.

References

[1] R. J. Coates, "Measurements of solar radiation and atmospheric attenuation at 4.3-millimeters wavelength," in *Proc. IRE*, Jan. 1958, pp. 122–126.

[2] S. M. Adler-Golden and J. R. Slusser, "Comparison of plotting methods for solar radiometer calibration," *J. Atmos. Oceanic Technol.*, vol. 24, pp. 935–938, 2007.

[3] C. U. Keller and S. Krucker, "Radio observations of the quiet sun," in *Solar and Space Weather Radiophysics*. New York, NY, USA: Springer, 2005, ch. 14, vol. 314, pp. 287–303. doi: 10.1007/1-4020-2814-8_14.

[4] F. S. Marzano, L. Milani, V. Mattioli, K. M. Magde, and G. A. Brost, "Retrieval of precipitation extinction using ground-based sun-tracking millimeter-wave radiometry, in *Proc. 2016 IEEE Int. Geosci. Remote Sens. Symp.*, Beijing, China, 2016, pp. 2162–2165. doi: 10.1109/IGARSS.2016.7729558.

[5] S. M. White and M. R. Kundu, "Solar observations with a millimeter-wavelength array," *Solar Phys.*, vol. 141, no. 2, pp. 347–369, Oct. 1992.

[6] H. Nakajima *et al.*, "The Nobeyama radioheliograph," *Proc. IEEE*, vol. 82, no. 5, pp. 705–713, 1994.

[7] K. Shibasaki, "Microwave observations of the quiet Sun," in *Proc. Nobeyama Symp. Solar Phys. Radio Observ.*, Kiyosato, Japan, Oct. 1998, pp. 1–9.

[8] K. Shibasaki, C. E. Alissandrakis, and S. Pohjolainen, "Radio emission of the quiet sun and active regions (invited review)," *Solar Phys.*, vol. 273, no. 2, pp. 309–337, Nov. 2011.

[9] C. Lindsey, G. Kopp, T. A. Clark, and G. Watt, "The sun in submillimeter and near-millimeter radiation," *Astrophys. J.*, vol. 453, pp. 511–516, Nov. 1995.

[10] D. L. Croom, "Sun as a broadband source for tropospheric attenuation measurements at millimetre wavelengths," *Proc. Inst. Electr. Eng.*, vol. 120, no. 10, pp. 1200–1206, Oct. 1973, doi: 10.1049/piee.1973.0244.

[11] D. C. Hogg and T.-S. Chu, "The role of rain in satellite communications," *Proc. IEEE*, vol. 63, no. 9, pp. 1308–1331, Sep. 1975. doi: 10.1109/PROC.1975.9940.

[12] K. Shimada, M. Higashiguchi, and Y. Otsu, "Characteristics of atmospheric attenuation at 35 GHz obtained by sun track measurements," *Electron. Commun. Japan*, vol. 67-B, no. 2, pp. 26–36, 1984.

[13] F. S. Marzano, V. Mattioli, L. Milani, K. M. Magde, and G. A. Brost, "Sun-tracking microwave radiometry: All-weather estimation of atmospheric path attenuation at Ka-, V-, and W-band, *IEEE Trans. Antennas Propag.*, vol. 64, no. 11, pp. 4815–4827, Nov. 2016. doi: 10.1109/TAP.2016.2606568.

[14] F. S. Marzano, E. Fionda, P. Ciotti, and A. Martellucci, "Ground-based multi-frequency microwave radiometry for rainfall remote sensing," *IEEE Trans. Geosci. Remote Sens.*, vol. 40, pp. 742–759, 2002.

[15] F. S. Marzano, E. Fionda, and P. Ciotti, "A neural network approach to precipitation intensity and extinction retrieval by ground-based passive microwave technique," *J. Hydrol.*, vol. 328, pp. 121–131, 2006. doi: 10.1016/j.hydrol.2005.11.42.

[16] F. S. Marzano, D. Cimini, P. Ciotti, and R. Ware, "Modeling and measurements of rainfall by ground-based multispectral microwave radiometry," *IEEE Trans. Geosci. Remote Sens.*, vol. 43, no. 5, pp. 1000–1011, May 2005.

[17] F. S. Marzano, "Predicting antenna noise temperature due to rain clouds at microwave and millimeter-wave frequencies," *IEEE Trans. Antennas Propag.*, vol. 55, no. 7, pp. 2022–2031, 2007.

[18] C. Ho, S. Slobin, A. Kantak, and S. Asmar, "Solar brightness temperature and corresponding antenna noise temperature at microwave frequencies," *JPL IPN Progress Report*, vol. 42-175, pp. 1–11, Nov. 2008.

[19] W. Graf, R. Bracewell, J. Deuter, and J. Rutherford, "The sun as a test source for boresight calibration of microwave antennas," *IEEE Trans. Antennas Propag.*, vol. 19, no. 5, pp. 606–612, Sep. 1971. doi: 10.1109/TAP.1971.1139996.

[20] F. T. Ulaby, R. K. Moore, and A. K. Fung, *Microwave Remote Sensing Active and Passive*. Reading, MA, USA: Addison, 1981, vol. 1, pp. 288–302.

[21] J. C. Liljegren, E. E. Clothiaux, G. G. Mace, S. Kato, and X. Dong, "A new retrieval for cloud liquid water path using a ground-based microwave radiometer and measurements of cloud temperature. *J. Geophys. Res.*, vol. 106, pp. 14 485–14 500, 2001.

[22] V. Mattioli, "Alphasat TDP5 GS G/T measurement campaign and IOT GS4-MWR, Graz, Austria: Definition of radiometric coefficients," Joanneum Research (DIG.03-12.AF.023-01 TN/111113-01, Graz, Austria), ESA/ESTEC Contract Number 4000102639/10/NL/CLP, Tech. Note TN-SCIEX-111113, pp. 20, Nov. 11, 2013.

[23] Radiometer Physics GmbH, "Technical instrument manual," Radiometer Physics GmbH, Meckenheim, Germany, Tech. Rep. RPG-MWR-STD-TM, Sep. 2013.

[24] J. E. McKay *et al.*, "Compact wideband corrugated feedhorns with ultra-low side lobes for very high performance antennas and quasi-optical systems," *IEEE Trans. Antennas Propag.*, vol. 61, no. 4, pp. 1714–1721, 2013. doi: 10.1109/TAP.2013.2243097.

[25] M. M. Franco, S. D. Slobin, and C. T. Stelzried, "20.7 and 31.4-GHz solar disk temperature measurements," Jet Propulsion Lab., California Inst. Technol., Pasadena, CA, USA, TDA Progress Report 42-64, 1981, pp. 140–168.

[26] J. L. Linsky, "A recalibration of the quiet Sun millimeter spectrum based on the Moon as an absolute radiometric standard," *Sol. Phys.*, vol. 28, pp. 419–424, 1973.

[27] H. C. Ko, "On the analysis of radio astronomical observations made with high resolution radio telescope antennas," Ohio State Univ., Columbus, OH, USA, Issue 21 of Radio Observatory report, 1961.

[28] F. Cuervo *et al.*, "Use of microwave profiler for Alphasat ALDO In-Orbit Tests and atmospheric observations," in *Proc. 8th Eur. Conf. Antennas Propag. (EuCAP 2014)*, The Hague, 2014, pp. 686–689, doi: 10.1109/EuCAP.2014.6901852.

[29] V. Mattioli, A. Graziani, P. Tortora, A. V. Bosisio, and L. Castanet, "Analysis and improvements of methodologies for discriminating atmospheric conditions from radiometric brightness temperatures," in *Proc. 7th Eur. Conf. Antennas Propag.*, 2013, pp. 1392–1396.

[30] A. V. Bosisio, G. Graziani, V. Mattioli, and P. Tortora, “On the use of microwave radiometers for deep space mission applications by means of a radiometric-based scalar indicator,” *IEEE J. Sel. Topics Appl. Earth Observ. Remote Sens.*, vol. 8, no. 9, pp. 4336–4344, Sep. 2015.

[31] J. A. Schroeder and E. R. Westwater, Users’ guide to WPL microwave radiative transfer software, NOAA/Environ. Res. Lab., Boulder, CO, USA, Tech. Rep. ERL-219 WPL-213, 1991, Art. no 84.

[32] P. W. Rosenkranz, “Correction to water vapor microwave continuum absorption: A comparison of measurements and models,” *Radio Sci.*, vol. 34, no. 4, 1999, Art. no. 1025.

[33] V. Mattioli, P. Basili, S. Bonafoni, P. Ciotti, and E. R. Westwater, “Analysis and improvements of cloud models for propagation studies,” *Radio Sci.*, vol. 44, Mar 2009, Art. no. RS2005. doi: 10.1029/2008RS003876.

[34] G. Brost and K. M. Magde, “On the use of the radiometer formula for atmospheric attenuation measurements at GHz frequencies,” in *Proc. 10th Eur. Conf. Antennas Propag.*, Davos, Switzerland, Apr. 2016, pp. 1–5.

[35] J. E. Vernazza, E. H. Avrett, and R. Loeser, “Structure of the solar chromosphere. III. Models of the EUV brightness components of the quit Sun,” *Astrophys. J. Suppl. Series*, vol. 45, pp. 635–725, Apr. 1981.

[36] V. Mattioli, F. S. Marzano, N. Pierdicca, C. Capsoni, and A. Martellucci, “Sky-noise temperature modelling and prediction for deep space applications from X Band To W band,” *IEEE Trans. Antennas Propag.*, vol. 61, no. 7, pp. 3859–3868, 2013.

[37] F. S. Marzano, “Modeling antenna noise temperature due to rain clouds at microwave and millimeter-wave frequencies,” *IEEE Trans. Antennas Propagat.*, vol. 54, no. 4, pp. 1305–1317, Apr. 2006.

[38] C. J. Willmott, S. M. Robesonb, and K. Matsuura, “A refined index of model performance,” *Int. J. Climatol.*, vol. 32, pp. 2088–2094, 2012.

[39] V. Meunier, U. Lohnert, P. Kollias, and S. Crewell, “Biases caused by the instrument bandwidth and beam width on simulated brightness temperature measurements from scanning microwave radiometers,” *Atmospheric Meas. Tech.*, vol. 6, pp. 1171–1187, 2013. doi:10.5194/amt-6-1171-2013.

[40] V. Mattioli, E. R. Westwater, D. Cimini, A. J. Gasiewski, M. Klein, and V. Y. Leuski, “Microwave and millimeter-wave radiometric and radiosonde observations in an arctic environment,” *AMS J. Atmospheric Oceanic Tech.*, vol. 25, no. 10, pp. 1768–1777, 2008. doi: 10.1175/2008JTECHA1078.1.

[41] H. Brogniez *et al.*, “review of sources of systematic errors and uncertainties in observations and simulations at 183 GHz,” *Atmospheric Meas. Tech.*, vol. 9, pp. 2207–2221, 2016. doi: 10.5194.

[42] X. Zou, L. Lin, and F. Weng, “Absolute calibration of ATMS upper level temperature sounding channels using GPS RO observations,” *IEEE Trans. Geosci. Remote Sens.*, vol. 52, no. 2, pp. 1397–1406, Feb. 2014. doi: 10.1109/TGRS.2013.2250981.

Vinia Mattioli (M’03) received the M.S. degree in electronic engineering and the Ph.D. degree in information engineering (thematic area: atmospheric remote sensing) from the University of Perugia, Perugia, Italy, in 2001 and 2005, respectively.

From 2005 to 2012, she was with the Department of Electronic and Information Engineering, University of Perugia, and with the Department of Information Engineering, Electronics and Telecommunications, Sapienza University of Rome, Italy, as a Postdoctorate Research Associate. Since 2013, she has been with EUMETSAT, Darmstadt, Germany, as a Calibration Consultant for EPS-SG MWI and ICI spaceborne radiometers. Between 2003 and 2004, she received the Ph.D. scholarship to conduct research at the Environmental Technology Laboratory, National Oceanic and Atmospheric Administration, Boulder, CO, USA, and between 2011 and 2012, she was Visiting Scientist at the Electromagnetics and Radar Department, Onera, Toulouse, France. She was MC Substitute Member of the COST Action IC0802. Her research interests include radiometer calibration techniques, passive ground-based and satellite-based microwave atmospheric remote sensing, physical and statistical modeling for radio propagation applications, microwave radiative transfer models, and GPS applied to remote sensing.

Luca Milani (M’16) received the B.Sc. (*cum laude*) and M.Sc. (*cum laude*) degrees in electronic engineering from Sapienza University of Rome, Rome, Italy, in 2013 and 2015, respectively.

From 2015 to 2016, he was with the European Space Agency/European Space Operations Centre, Darmstadt, Germany, on deep space communication links and data processing. In 2016, he joined the Department of Information Engineering, Electronics and Telecommunications, University of Rome “La Sapienza”, Italy. His current research interests include ground-based and space-based microwave radiometry and atmospheric radiopropagation at Ka band, and above.

Kevin M. Magde received the B.Sc. degree in computer engineering from the Rochester Institute of Technology, Rochester, NY, USA, in 1987, and the M.Sc. degree in electrical engineering from Syracuse University, Syracuse, NY, USA, in 1994.

He has been working on in-house projects for the USAF, since 1985. From 1985 to 2005 consisted of research in the field of optics, and during 2005 to 2010 work on radar signal processing was performed. Currently, he works in a group concerned with using radiometers to measure attenuation statistics in the V/W-band.

George A. Brost received the Ph.D. degree in physics from Washington State University, Pullman, WA, USA, in 1984.

From 1984 to 1988, he was a NRC Post Doctorate Fellow and Visiting Scientist at F. J. Seiler Research Lab, USAF Academy. Since 1988, he has been with the Air Force Research Laboratory in, Rome, NY, USA. His research has encompassed a broad range of activities involving the propagation and interaction of electromagnetic waves with matter. His current research interests include the development of advanced satellite communications technology with a focus on propagation and atmospheric effects on millimeter waves.

Frank S. Marzano (S’89–M’99–SM’03–F’16) received the Laurea degree (*cum laude*) in electrical engineering and the Ph.D. degree in applied electromagnetics both from the University of Rome “La Sapienza,” Rome, Italy, in 1988 and 1993, respectively.

In 1992, he was a Visiting Scientist at Florida State University, Tallahassee, FL. During 1993, he collaborated with the Institute of Atmospheric Physics, National Council of Research, Rome, Italy. From 1994 to 1996, he was with the Italian Space Agency, Rome, Italy, as a Postdoctorate Researcher. After being a Lecturer at the University of Perugia, Italy, in 1997 he joined the Department of Electrical Engineering, University of L’Aquila, Italy teaching courses on electromagnetic fields as Assistant Professor. In 1999, he was at Naval Research Laboratory, Monterey, CA, as a Visiting Scientist. In 2002, he got the qualification to Associate Professorship and has cofounded the Center of Excellence on Remote Sensing and Hydro-Meteorological Modeling (CETEMPS), L’Aquila. In 2005, he finally joined the Department of Information engineering, Electronics and Telecommunications, Sapienza University of Rome, Rome, Italy where he presently teaches courses on antennas, propagation, and remote sensing. Since 2007, he has been a Vice-Director of CETEMPS, University of L’Aquila, L’Aquila, Italy where he became Director in 2013. His current research interests include passive and active remote sensing of the atmosphere from ground-based, airborne, and space-borne platforms and electromagnetic propagation studies.

Dr. Marzano has published more than 130 papers on refereed International Journals, more than 30 contributions to international Book chapters, and more than 300 extended abstract on international and national congress proceedings. He was the Editor of two books. Since January 2004, he has been acting as an Associated Editor of the IEEE GEOSCIENCE REMOTE SENSING LETTERS. In 2005 and 2007, he was Guest Coeditor of the MicroRad04 and MicroRad06 Special Issues for IEEE-GRSL. Since January 2011, he has been an Associate Editor of the journal *EGU Atmospheric Measurements Techniques*. He is a Fellow the UK Royal Meteorological Society as well as member of the MWI-ICI Science Advisory Group of EUMETSAT, and the GPM Science Team of NASA.